GEOLOGY | THE GEOLOGICAL SOCIETY OF AMERICA®

https://doi.org/10.1130/G52655.1

Manuscript received 1 August 2024
Revised manuscript received 3 September 2024
Manuscript accepted 13 September 2024

Published online 4 October 2024

Diachronous end-Permian terrestrial crises in North and South China

Daoliang Chu[1,*], Haijun Song[1], Jacopo Dal Corso[1], A.M.E. Winguth[2], Mitali D. Gautam[2], Paul B. Wignall[3], Stephen E. Grasby[4], Wenchao Shu[1], Hanchen Song[1], Huyue Song[1], Li Tian[1], Yuyang Wu[1], and Jinnan Tong[1]

[1]State Key Laboratory of Biogeology and Environmental Geology, School of Earth Sciences, China University of Geosciences, Wuhan 430074, China
[2]Department of Earth and Environmental Sciences, University of Texas at Arlington, Arlington, Texas 76019, USA
[3]School of Earth and Environment, University of Leeds, Leeds LS2 9JT, UK
[4]Geological Survey of Canada, Natural Resources Canada, Calgary, Alberta T2L 2A7, Canada

ABSTRACT

Climate breakdown driven by massive volcanic eruptions was the likely cause of the terrestrial Permian–Triassic mass extinction (ca. 252 Ma). However, establishing the relationship between climate factors and terrestrial ecosystem responses is difficult. Furthermore, it is unclear if the pattern and timing of the terrestrial ecosystem crises are consistent across different regions. Our integrated paleontology and geochemistry study indicates that the onset of the terrestrial crisis in North China preceded that in South China by at least 300 k.y. Geological and Earth system modeling suggest that lethal heatwaves and aridity, along with enhanced climate seasonality, were caused by higher atmospheric CO_2. The onset of these environmental changes varied regionally and were likely responsible for the diachronous terrestrial crisis. Our results indicate that, rather than a globally synchronous event, cumulative regional extirpations ultimately resulted in a global terrestrial extinction.

INTRODUCTION

In addition to being a marine catastrophe, the Permian–Triassic mass extinction (PTME) was also a major crisis of terrestrial ecosystems (e.g., Dal Corso et al., 2022). Terrestrial plants suffered global losses (Hermann et al., 2011; Cascales-Miñana et al., 2016; Vajda et al., 2020), and there is an Early–Middle Triassic "coal gap" caused by the loss of peat-forming flora (Retallack et al., 1996). The terrestrial crisis reportedly occurred over a relatively long interval, but it is unclear whether it was a uniform catastrophic event or a more gradual process, and its driving mechanisms remain debated (Fielding et al., 2019; Chu et al., 2020; Gastaldo et al., 2020; Vajda et al., 2023). The consensus links the causes of the PTME to volatile emissions from the Siberian Traps large igneous province with possible additional contributions from continental arc volcanism (Yin et al., 1992; Wignall, 2015; Zhang et al., 2021). Injections of CO_2, SO_2, and halogens into the atmosphere are thought to have led to extreme global climatic conditions (e.g., Joachimski et al., 2012; Black et al., 2014). The links between climatic and/or environmental factors and extinction are well established in marine successions, but defining the causal relationships in terrestrial settings is challenging because high-resolution terrestrial studies and quantitative paleoclimate proxies are limited.

We have determined the timing and processes of the terrestrial biotic crisis through paleontological and geochemical analyses from different paleolatitudes. Our findings indicate that the onset of the terrestrial crisis in North China preceded that in South China, a conclusion that can be matched with the simulation results of the Community Climate System Model (CCSM 3.0) (Collins et al., 2006; Winguth et al., 2015; https://www.cesm.ucar.edu/models/ccsm).

MATERIALS AND METHODS

We examined four Permian–Triassic boundary sections in North and South China (Fig. 1): at Dayulin (34.48504°N, 112.18245°E; Henan Province) and Shichuanhe (35.02917°N, 108.87833°E; Shaanxi Province) sections in North China, which lay at a paleolatitude of ~20°N; and the Chinahe (26.13077°N, 104.35637°E; Yunnan Province) and Chahe (26.72054°N, 103.82125°E; Guizhou Province) sections from South China, at a paleoequatorial location (Muttoni et al., 2009). The Dayulin and Shichuanhe sections encompass the Permian–Triassic transition in the Sunjiagou Formation and the Early Triassic Liujiagou Formation. The Chinahe and Chahe sections encompass the latest Permian Xuanwei Formation, the Permian–Triassic transitional Kayitou Formation, and the earliest Triassic Dongchuan Formation. New plant macrofossils were sought bed by bed as a complement to previous collection efforts. Palynomorphs were extracted from mudstone samples using palynological acid maceration techniques. Hg content was measured using a Lumex RA-915 mercury analyzer coupled to a PYRO-915+ pyrolyzer. Al_2O_3 contents were measured using a Zsx Primus II wavelength dispersive X-ray fluorescence spectrometer (XRF). CCSM 3.0 was used to simulate the surface air temperature (SAT) and precipitation of the studied areas. Detailed laboratory methods and palaeoclimate modeling processes are given in the Supplemental Material[1].

RESULTS

Paleontology

At the Dayulin section, a plant fossil assemblage dominated by *Pseudovoltzia*-type and *Ullmannia*-type conifers and pollen dominated by *Lueckisporites virkkiae* and *Lunatisporites* spp.

Daoliang Chu https://orcid.org/0000-0002-2261-5597
*chudl@cug.edu.cn

[1]Supplemental Material. Description of the analytical methods, supplemental figures, and data tables. Please visit https://doi.org/10.1130/GEOL.S.27075898 to access the supplemental material; contact editing@geosociety.org with any questions.

CITATION: Chu, D., et al., 2025, Diachronous end-Permian terrestrial crises in North and South China: Geology, v. 53, p. 55–60, https://doi.org/10.1130/G52655.1

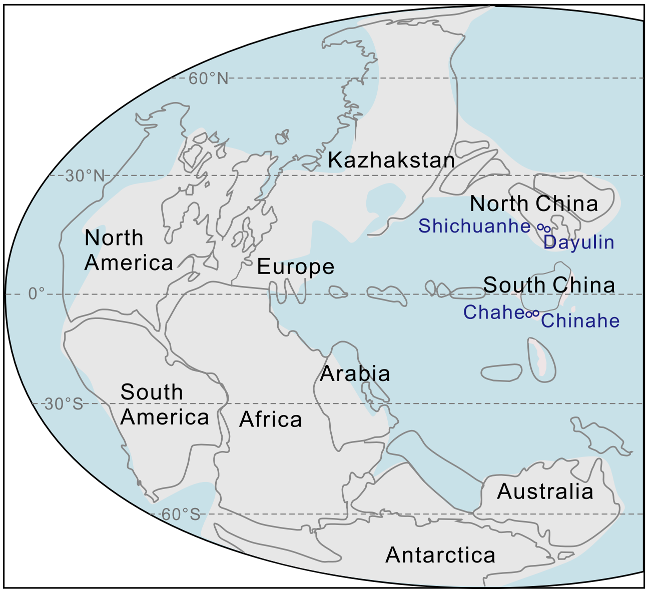

Figure 1. Late Permian to Early Triassic paleogeographic map showing locations of the studied sections (in blue) (base map after Muttoni et al., 2009).

were collected in the lower part of the Sunjiagou Formation (Figs. S1 and S2 in the Supplemental Material). No plant macrofossils were discovered above 25.5 m in the Dayulin section (Fig. 2A). At the Shichuanhe section, a diverse ichnoassemblage was discovered in the lower part of the Sunjiagou Formation, but no trace fossils are found above 30 m (Fig. 2E).

At the Chinahe section, a rainforest-type *Gigantopteris* flora was collected in the coal-bearing Xuanwei Formation (Fig. 2H), dominated by gigantopterid and pecopterid leaves (Fig. S1). Thereafter, this vegetation is replaced by a monotonous plant fossil assemblage consisting of small peltasperm and lycophyte species at the base of the Kayitou Formation (Fig. 2H). Abundant trilete azonate and monolete spores, typically produced by pteridophytes, were recovered from the Xuanwei Formation and the base of the Kayitou Formation (Fig. 2I; Fig. S2). Throughout the succeeding palynomorph assemblages at 3–5 m above the basal Kayitou Formation, *Aratrisporites* and trilete zonate become the dominant spores, and non-striate bisaccate pollens gradually increase. Charcoal abundance increases significantly at this interval (Fig. 2J). Above this level, abundant non-striate bisaccate pollen (mostly *Alisporites*) dominate while spores decrease (Fig. 2I). At the Chahe section, the *Gigantopteris* flora experienced a decrease in diversity coinciding with rapid rises of charcoal abundance in the lower part of the Kayitou Formation (Figs. 2N and 2O).

Sedimentology

The Chinahe and Chahe locations record predominantly low-energy, coastal swamp conditions, and five lithofacies occur during the Permian–Triassic boundary interval (Fig. S3). The absence of wave processes points to a sheltered setting, while sharp-based, coarse chamositic sand with charcoal detritus records major flood events, suggesting a flashy discharge regime in the coastal rivers (Wignall et al., 2020). In the Dayulin and Shichuanhe sections, the middle part of the Sunjiagou Formation consists of packages of dark red muddy siltstone with bands of paleosols and fine-grained sandstone. Aridisols, evidenced by calcareous nodules 2–10 cm in diameter, are the main paleosol type (Fig. S4). This is interpreted to record an alluvial floodplain facies dominated by mud deposition and soil formation in a generally dry climate (Ji et al., 2023).

Organic Carbon Isotopes ($\delta^{13}C_{org}$) and Mercury (Hg)

After a gradual decline, an abrupt negative carbon isotope excursion (NCIE) of ~3‰–5‰ in $\delta^{13}C_{org}$ occurs in the middle part of the Sunjiagou Formation at the Dayulin and Shichuanhe sections and in the lower part of the the Kayitou Formation at the Chinahe and Chahe sections. Hg concentrations at Dayulin show low values in the lower Sunjiagou Formation, with peaks at 50–70 m (Fig. 2D). Hg contents at Shichuanhe show the same trend, with a peak of 51 ppb at 48 m (Fig. 2G). Both total organic carbon (TOC) and total sulfur (TS) at Dayulin and Shichuanhe are too low to be used for Hg/TOC or Hg/TS normalization. Hg/Al_2O_3 shows the same trend as Hg content. However, the weak correlation between Hg and Al_2O_3 concentrations (R^2 <0.01, P >0.05) suggests that the Hg fluctuations are not affected by changes in clay content. There is a similar trend in Chinahe and Chahe, where a sudden rise in Hg and Hg/TOC or Hg/Al_2O_3 at the bottom of the Kaitou Formation was observed (Figs. 2M and 2Q; Fig. S5). All four sections show that the onset of the increased Hg contents is within the nadir of the NCIE.

Climate Modeling

CCSM 3.0 climate sensitivity experiments provide surface air temperature (SAT) and precipitation differences between 4× and 12× preindustrial pCO_2 scenarios (Fig. 3), potentially representing the pre-extinction latest Permian and Permian–Triassic boundary conditions (Kidder and Worsley, 2004; Wu et al., 2021). Lower cloud optical depth, i.e., thinner clouds, was considered in the 12× CO_2 simulation, due to biophysical-climate feedbacks under higher pCO_2, which more closely matches the biomass decline during the extinction event and its aftermath (Winguth et al., 2015). The results show that seasonality increased across the PTME in North China, annual mean SAT increased by 8–10 °C (Fig. 3C), and the maximum SAT exceeded 42 °C (Fig. 3B). Annual precipitation minus evaporation increased slightly from the latest Permian to Early Triassic (Fig. S6). Meanwhile, precipitation seasonality increased in South China, although precipitation minus evaporation significantly increased across the PTME (Fig. S7). Both annual mean and maximum SATs increased by 6–7 °C, and the maximum SAT was ~38 °C in South China (Figs. 3B and 3C).

DISCUSSION

Diachronous End-Permian Terrestrial Crises

The end-Permian terrestrial crisis at the Dayulin section (North China), characterized by the disappearance of plants and TOC decline, occurred during a gradual fall of $\delta^{13}C_{org}$ (Fig. 4). The loss of bioturbation at the Shichuanhe section also predates the onset of the abrupt NCIE, which was calibrated to 252.21 ± 0.15 Ma (Guo et al., 2022). At the Chinahe and Chahe sections (South China), the loss of the *Gigantopteris* flora and increased charcoal abundance occurs at the base of the Kayitou Formation and coincides with the abrupt onset of the NCIE, which began immediately above a volcanic ash bed dated to 251.884 ± 0.052 Ma (Wu et al., 2024). The subsequent significant decrease in TOC coincides with the nadir of the NCIE and corresponds to the horizon of the first Hg peak at Chinahe (Fig. 2). Multiple episodes of Hg enrichments occured during the PTME; these episodes could record major pulses of felsic volcanism in the region and in the Siberian Traps large igneous province (e.g., Edward et al., 2023). However, there are major Hg anomalies, consistent with the nadir of the NCIE, which are seen globally in both terrestrial and marine successions (e.g., Grasby et al., 2017; Chu et al., 2020; Edward et al., 2023) that serve as a useful correlation tool. Hence, the paleontological, geochemical, and geochronological data show that the terrestrial crisis in North China occurred ~300 k.y. before that of the tropical rainforests in South China (Fig. 4).

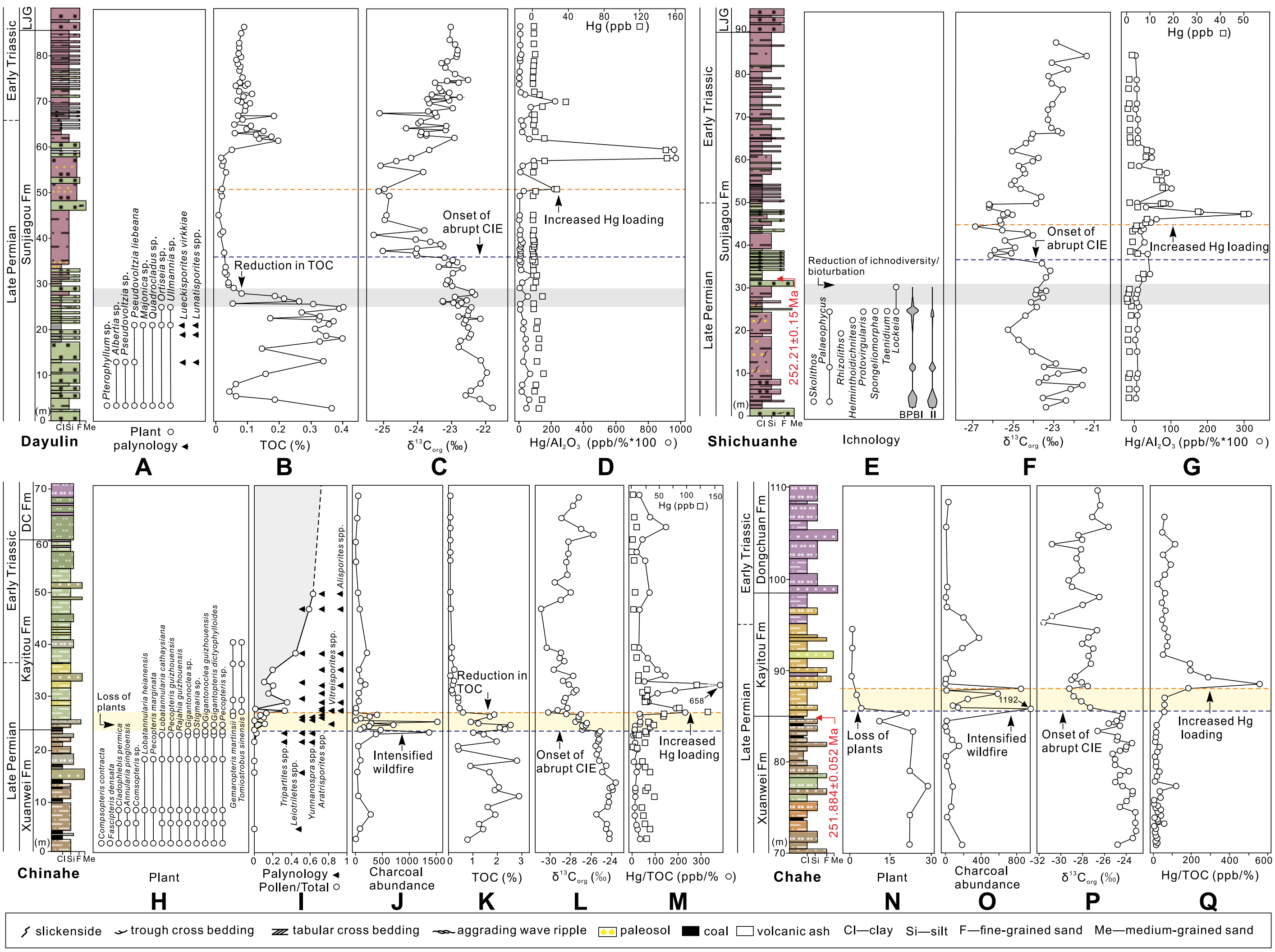

Figure 2. Stratigraphy, plant fossils, palynology, charcoal abundance, total organic carbon (TOC), organic carbon isotopes ($\delta^{13}C_{org}$), and Hg concentration in the studied four sections in North and South China. Logs show lithologies with approximate representation of color. DC Fm—Dongchuan Formation; LJF Fm—Liujiagou Formation; CIE—carbon isotope excursion. (A–D) Dayulin section in the China. (A) Plant fossil and palynology distribution. The arrowheads show occurrences of the specific sporopollens. (B) TOC values (Wu et al., 2020). (C) $\delta^{13}C_{org}$ (Wu et al., 2020). (D) Vertical trends in Hg contents and Hg/Al_2O_3 ratios. (E–G) Shichuanhe section in North China. (E) Ichnology distribution. BPBI—bedding plane bioturbation index. II—ichnofabric index. (F) $\delta^{13}C_{org}$ (Wu et al., 2020). (G) Hg contents and Hg/Al_2O_3 ratios. (H–M) Chinahe section in South China. (H) Plant fossil distribution. (I) Palynology and the ratio of pollen to total spores (Table S4 [see text footnote 1]). Arrowheads show occurrences of specific sporopollens. Pollen/total ratio means the ratio of the pollen count to the total number of spores and pollen; it can represent climate change to a certain extent, and a higher pollen content may indicate drought. (J) Charcoal abundance (particles per 100 g bulk rock). (K) TOC. (L) $\delta^{13}C_{org}$. (M) Hg concentration and Hg/TOC ratios. (N–Q) Chahe section in South China. (N) Plant fossil diversity changes. (O) Charcoal abundance. (P) $\delta^{13}C_{org}$ (Shen et al., 2011). (Q) Hg/TOC ratio (Wang et al., 2021). Data in panels J–M are from Chu et al. (2020). High-precision U-Pb geochronological data are from Guo et al. (2022) and Wu et al. (2024).

Lethal Warming and Enhanced Seasonality

In C_3 plants, photorespiration replaces photosynthesis above 35 °C, and only a few plants can survive above 40 °C (Sage and Kubien, 2007). The negative effects of heat stress are exacerbated by drought and can result in tree mortality (Teskey et al., 2015). Respiratory evaporative water loss is significantly increased in most terrestrial animals at temperatures above 35–40 °C, and temperatures of 40 °C or higher causes protein damage (Somero, 1995). Simulations show that the average annual temperature in North China increased by 8–10 °C (Fig. 3C), with highest temperature >42 °C, during the end-Permian terrestrial crisis due to the combined effects of high CO_2 greenhouse forcing and reduced cloud cover (Fig. 3B). This surpasses the tolerance limits of most plants and terrestrial animals. Although annual precipitation minus evaporation slightly increased, there was a higher frequency of months where evaporation exceeded precipitation (Figs. 3I–3K), such that more seasonal precipitation was combined with more prolonged drought. The occurrence of floodplain facies and calcareous nodules in aridisols is consistent with an overall dry climate with intermittent periods of substantial rainfall (Ji et al., 2023). Therefore, in North China, a lethal combination of heatwaves and prolonged drought could lead to a severe terrestrial ecosystem crisis.

In South China, rainforest plants were replaced by peltasperms and lycophytes, which have a higher tolerance to climatic variability (Feng et al., 2020). An ecological shift to flora with lower moisture dependencies is indicated by increases of *Alisporites*-dominated (produced by gymnosperms) pollen content. Meanwhile, increased wildfire activity and flood events occurred, indicating a transition from persistent humidity to unstable climatic conditions with prolonged dry periods (Figs. 2J and 2Q; Bercovici et al., 2015; Chu et al., 2020). Modeling also shows the same trend of overall higher, but more seasonal precipitation, particularly in the short term where evaporation exceeds precipitation

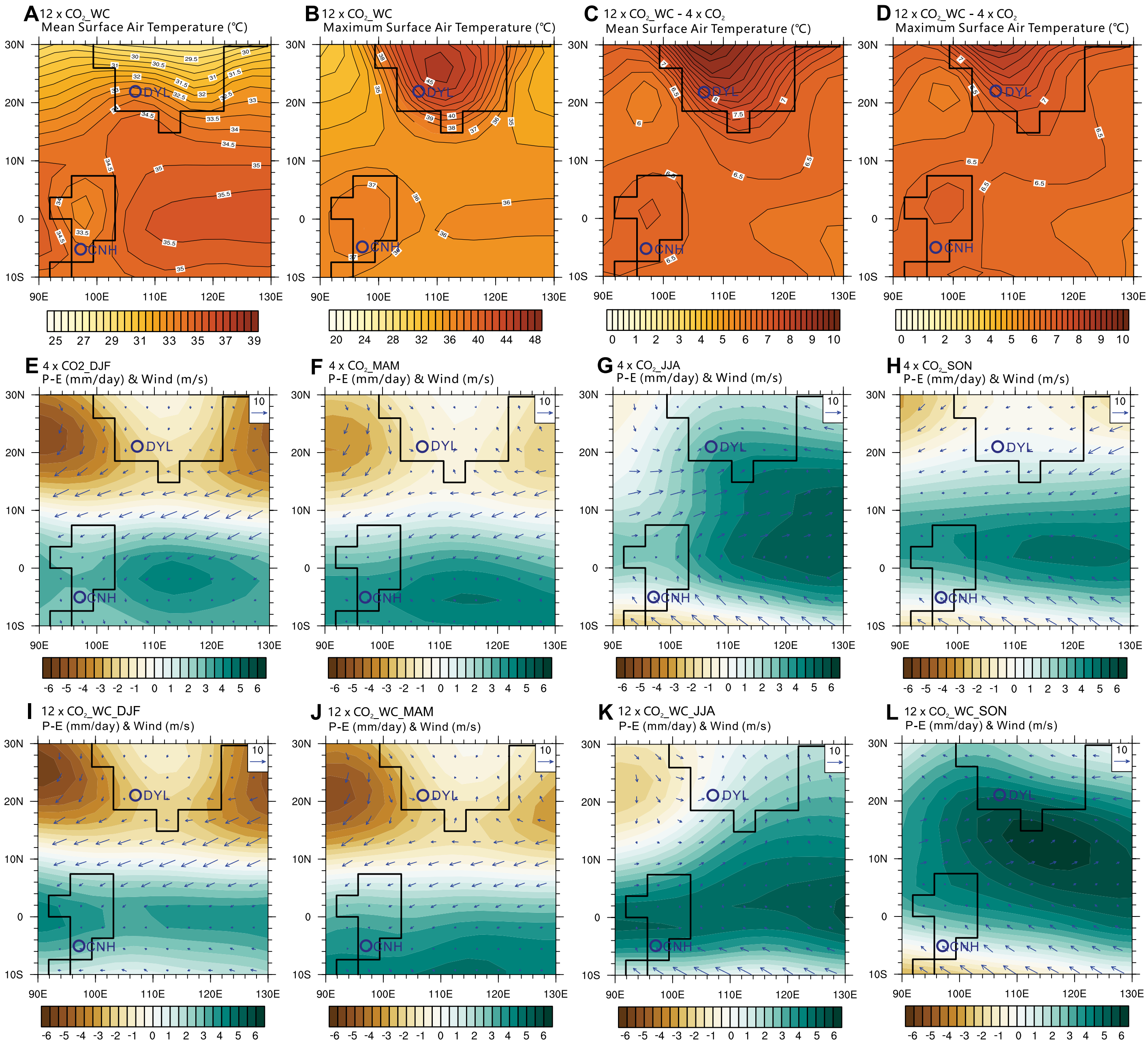

Figure 3. Community Climate System Model (version 3; Collins et al., 2006; Winguth et al., 2015; https://www.cesm.ucar.edu/models/ccsm) simulations of North and South China at the end-Permian mass extinction. DYL—Dayulin section in North China; CNH—Chinahe section in South China; WC—warm climate. (A–D) Annual mean (A) and maximum (B) surface air temperature in 12× preindustrial *p*CO_2 scenarios, and the differences between 12× and 4× preindustrial *p*CO_2 scenarios (C, D). (E–L) Seasonal precipitation minus evaporation (P - E; colored shading) and surface wind speed and direction (arrows) in 4× preindustrial *p*CO_2 scenarios (E–H) and 12× preindustrial *p*CO_2 scenarios. (I–L). Four boreal meteorological seasons: DJF—December, January, February (winter); MAM—March, April, May (spring); JJA—June, July, August (summer); SON—September, October, November (fall).

(Figs. 3I–3L). Furthermore, annual surface air temperature rose by 6–7 °C (Fig. 3C), peaking at 38 °C (Fig. 3B), inducing heat stress on the rainforest. Therefore, in South China, enhanced seasonal precipitation and heat stress were very likely key factors causing rainforest collapse.

In summary, sensitivity simulations and geological evidence point to elevated temperatures and heightened climate seasonality in South and North China during the end-Permian terrestrial crisis. Modeling shows that North China experienced more significant and severe climate changes compared to South China (Fig. 3). This may have caused an earlier crisis of the conifer-dominated flora compared to the later loss of tropical rainforests. Higher temperature increases (∼10–14 °C) and intensified seasonality likely contributed to the even earlier plant die-off in the high-latitude southeastern margin of Gondwana, which occurred ∼370 k.y. prior to the marine extinction (Fielding et al., 2019; Mays et al., 2020; Frank et al., 2021).

CONCLUSIONS

The Hg content, $\delta^{13}C_{org}$, and zircon U-Pb date data allowed correlation of terrestrial crises in South and North China and demonstrate non-synchroneity. Modeling and sedimentary records indicate that the crisis of conifers in low-latitude North China was primarily caused by extreme high temperatures and drought, driven by increasing *p*CO_2. In equatorial South China, the rainforest flora was affected by wildfires, while the paleobotanical record suggests the

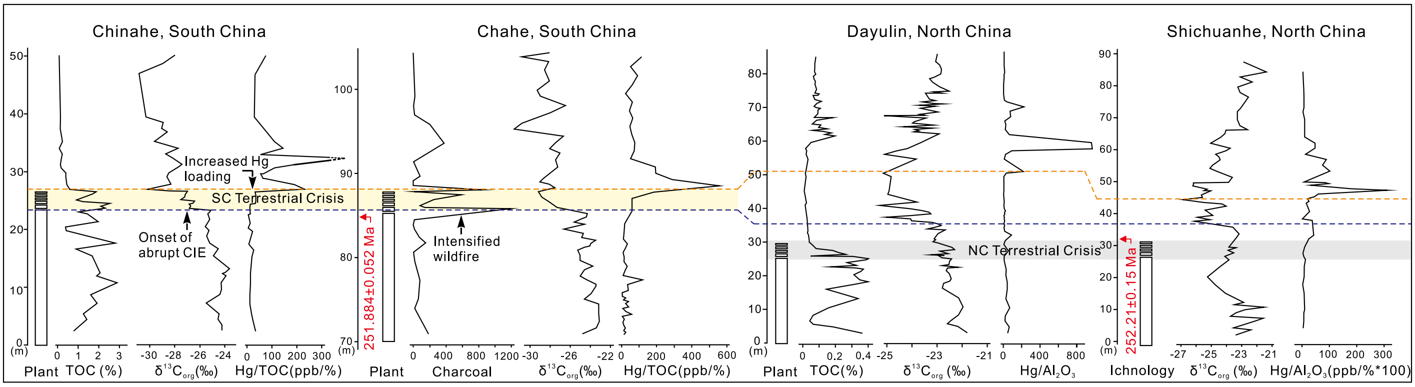

Figure 4. Total organic carbon (TOC), organic carbon isotopes ($\delta^{13}C_{org}$), U/Pb age, Hg/TOC or Hg/Al_2O_3, charcoal, and crisis interval correlations between the studied sections in North and South China. Yellow and gray zones show intervals of terrestrial crisis in South China (SC) and North China (NC). The column labeled "Plant" signifies the plant macrofossil occurrence. CIE—carbon isotope excursion.

presence of plants with lower moisture dependence. These observations indicate a transition from a stable, humid climate to a more seasonal climate across the extinction in South China, which is supported by simulation results indicating enhanced seasonal precipitation. The combination of extreme high temperatures and more severe drought in North China led to a scarcity of available moisture for plants. These factors likely contributed to the earlier terrestrial ecological crisis and limited survival of plants in North China.

ACKNOWLEDGMENTS

We thank C. Fielding and three anonymous reviewers for helpful comments. This study was supported by the National Natural Science Foundation of China (grants 92255303, 42030513, 42325202, and 42072025). Arne Winguth's research activity was supported by National Science Foundation grant EAR1636629. We would like to acknowledge high-performance computing support from Cheyenne (doi:10.5065/D6RX99HX) provided by the National Center for Atmospheric Research (NCAR) Computational and Information Systems Laboratory.

REFERENCES CITED

Bercovici, A., Cui, Y., Forel, M., Yu, J., and Vajda, V., 2015, Terrestrial paleoenvironment characterization across the Permian–Triassic boundary in South China: Journal of Asian Earth Sciences, v. 98, p. 225–246, https://doi.org/10.1016/j.jseaes.2014.11.016.

Black, B.A., Lamarque, J.F., Shields, C.A., Elkins-Tanton, L.T., and Kiehl, J.T., 2014, Acid rain and ozone depletion from pulsed Siberian Traps magmatism: Geology, v. 42, p. 67–70, https://doi.org/10.1130/G34875.1.

Cascales-Miñana, B., Diez, J.B., Gerrienne, P., and Cleal, C.J., 2016, A palaeobotanical perspective on the great end-Permian biotic crisis: Historical Biology, v. 28, p. 1066–1074, http://dx.doi.org/10.1080/08912963.2015.1103237.

Chu, D., et al., 2020, Ecological disturbance in tropical peatlands prior to marine Permian-Triassic mass extinction: Geology, v. 48, p. 288–292, https://doi.org/10.1130/G46631.1.

Collins, W.D., et al., 2006, The Community Climate System Model Version 3 (CCSM3): Journal of Climate, v. 19, p. 2122–2143, https://doi.org/10.1175/JCLI3761.1.

Dal Corso, J., Song, H., Callegaro, S., Chu, D., Sun, Y., Hilton, J., Grasby, S.E., Joachimski, M.M., and Wignall, P.B., 2022, Environmental crises at the Permian–Triassic mass extinction: Nature Reviews: Earth & Environment, v. 3, p. 197–214, https://doi.org/10.1038/s43017-021-00259-4.

Edward, O., Paul, A.N., Bucher, H., Vérard, C., Adatte, T., Sonke, J.E., Schaltegger, U., and Vennemann, T., 2023, Timing and provenance of volcanic fluxes around the Permian-Triassic boundary mass extinction in South China: U-Pb zircon geochronology, volcanic ash geochemistry and mercury isotopes: Geochemistry, Geophysics, Geosystems, v. 24, https://doi.org/10.1029/2023GC010912.

Feng, Z., Wei, H.-B., Guo, Y., He, X.-Y., Sui, Q., Zhou, Y., Liu, H.-Y., Gou, X.-D., and Lv, Y., 2020, From rainforest to herbland: New insights into land plant responses to the end-Permian mass extinction: Earth-Science Reviews, v. 204, https://doi.org/10.1016/j.earscirev.2020.103153.

Fielding, C.R., et al., 2019, Age and pattern of the southern high-latitude continental end-Permian extinction constrained by multiproxy analysis: Nature Communications, v. 10, 385, https://doi.org/10.1038/s41467-018-07934-z.

Frank, T.D., et al., 2021, Pace, magnitude, and nature of terrestrial climate change through the end-Permian extinction in southeastern Gondwana: Geology, v. 49, p. 1089–1095, https://doi.org/10.1130/G48795.1.

Gastaldo, R.A., Kamo, S.L., Neveling, J., Geissman, J.W., Looy, C.V., and Martini, A.M., 2020, The base of the *Lystrosaurus* Assemblage Zone, Karoo Basin, predates the end-Permian marine extinction: Nature Communications, v. 11, 1428, https://doi.org/10.1038/s41467-020-15243-7.

Grasby, S.E., Shen, W., Yin, R., Gleason, J.D., Blum, J.D., Lepak, R.F., Hurley, J.P., and Beauchamp, B., 2017, Isotopic signatures of mercury contamination in latest Permian oceans: Geology, v. 45, p. 55–58, https://doi.org/10.1130/G38487.1.

Guo, W., Tong, J., He, Q., Hounslow, M.W., Song, H., Dal Corso, J., Wignall, P.B., Ramezani, J., Tian, L., and Chu, D., 2022, Late Permian–Middle Triassic magnetostratigraphy in North China and its implications for terrestrial-marine correlations: Earth and Planetary Science Letters, v. 585, https://doi.org/10.1016/j.epsl.2022.117519.

Hermann, E., Hochuli, P.A., Bucher, H., Brühwiler, T., Hautmann, M., Ware, D., and Roohi, G., 2011, Terrestrial ecosystems on North Gondwana following the end-Permian mass extinction: Gondwana Research, v. 20, p. 630–637, https://doi.org/10.1016/j.gr.2011.01.008.

Ji, K., Wignall, P.B., Tong, J., Yu, Y., Guo, W., Shu, W., and Chu, D., 2023, Sedimentology of the latest Permian to Early Triassic in the terrestrial settings of the North China Basin: Low-latitude climate change during a warming-driven crisis: Geological Society of America Bulletin, v. 135, p. 481–503, https://doi.org/10.1130/B36260.1.

Joachimski, M.M., Lai, X., Shen, S., Jiang, H., Luo, G., Chen, B., Chen, J., and Sun, Y., 2012, Climate warming in the latest Permian and the Permian-Triassic mass extinction: Geology, v. 40, p. 195–198, https://doi.org/10.1130/G32707.1.

Kidder, D.L., and Worsley, T.R., 2004, Causes and consequences of extreme Permo-Triassic warming to globally equable climate and relation to the Permo-Triassic extinction and recovery: Palaeogeography, Palaeoclimatology, Palaeoecology, v. 203, p. 207–237, https://doi.org/10.1016/S0031-0182(03)00667-9.

Mays, C., Vajda, V., Frank, T.D., Fielding, C.R., Nicoll, R.S., Tevyaw, A.P., and McLoughlin, S., 2020, Refined Permian–Triassic floristic timeline reveals early collapse and delayed recovery of south polar terrestrial ecosystems: Geological Society of America Bulletin, v. 132, p. 1489–1513, https://doi.org/10.1130/B35355.1.

Muttoni, G., Gaetani, M., Kent, D.V., Sciunnach, D., Angiolini, L., Berra, F., Garzanti, E., Mattei, M., and Zanchi, A., 2009, Opening of the Neo-Tethys Ocean and the Pangea B to Pangea A transformation during the Permian: GeoArabia, v. 14, p. 17–48, https://doi.org/10.2113/geoarabia140417.

Retallack, G.J., Veevers, J.J., and Morante, R., 1996, Global coal gap between Permian–Triassic extinction and Middle Triassic recovery of peat-forming plants: Geological Society of America Bulletin, v. 108, p. 195–207, https://doi.org/10.1130/0016-7606(1996)108<0195:GCGBPT>2.3.CO;2.

Sage, R.F., and Kubien, D.S., 2007, The temperature response of C_3 and C_4 photosynthesis: Plant, Cell & Environment, v. 30, p. 1086–1106, https://doi.org/10.1111/j.1365-3040.2007.01682.x.

Shen, S.-Z., et al., 2011, Calibrating the end-Permian mass extinction: Science, v. 334, p. 1367–1372, https://doi.org/10.1126/science.1213454.

Somero, G.N., 1995, Proteins and temperature: Annual Review of Physiology, v. 57, p. 43–68, https://doi.org/10.1146/annurev.ph.57.030195.000355.

Teskey, R., Wertin, T., Bauweraerts, I., Ameye, M., McGuire, M.A., and Steppe, K., 2015, Responses of tree species to heat waves and extreme heat events: Plant, Cell & Environment, v. 38, p. 1699–1712, https://doi.org/10.1111/pce.12417.

Vajda, V., McLoughlin, S., Mays, C., Frank, T.D., Fielding, C.R., Tevyaw, A., Lehsten, V., Bocking, M., and Nicoll, R.S., 2020, End-Permian (252 Mya) deforestation, wildfires and flooding—An ancient biotic crisis with lessons for the present: Earth and Planetary Science Letters, v. 529, https://doi.org/10.1016/j.epsl.2019.115875.

Vajda, V., Grice, K., Krüger, A., Lee, S., and Shi, G.R., 2023, End-Permian marine ecosystem collapse was a direct consequence of deforestation: Evidence from the Kockatea Shale of the Perth Basin, Western Australia: Evolving Earth, v. 1, https://doi.org/10.1016/j.eve.2023.100027.

Wang, X., Cawood, P.A., Grasby, S.E., Zhao, L., Chen, Z.-Q., Wu, S., and Huang, Y., 2021, Characteristics of Hg concentrations and isotopes in terrestrial and marine facies across the end-Permian mass extinction: Global and Planetary Change, v. 205, https://doi.org/10.1016/j.gloplacha.2021.103592.

Wignall, P.B., 2015, The Worst of Times: How Life on Earth Survived Eighty Million Years of Extinction: Princeton, New Jersey, Princeton University Press, 224 p., https://doi.org/10.2307/j.ctvc77862.

Wignall, P.B., Chu, D., Hilton, J.M., Dal Corso, J., Wu, Y., Wang, Y., Atkinson, J., and Tong, J., 2020, Death in the shallows: The record of Permo-Triassic mass extinction in paralic settings, southwest China: Global and Planetary Change, v. 189, https://doi.org/10.1016/j.gloplacha.2020.103176.

Winguth, A.M.E., Shields, C.A., and Winguth, C., 2015, Transition into a hothouse world at the Permian-Triassic boundary—A model study: Palaeogeography, Palaeoclimatology, Palaeoecology, v. 440, p. 316–327, https://doi.org/10.1016/j.palaeo.2015.09.008.

Wu, Q., et al., 2024, The terrestrial end-Permian mass extinction in the paleotropics postdates the marine extinction: Science Advances, v. 10, https://doi.org/10.1126/sciadv.adi7284.

Wu, Y., Tong, J., Algeo, T.J., Chu, D., Cui, Y., Song, H., Shu, W., and Du, Y., 2020, Organic carbon isotopes in terrestrial Permian-Triassic boundary sections of North China: Implications for global carbon cycle perturbations: Geological Society of America Bulletin, v. 132, p. 1106–1118, https://doi.org/10.1130/B35228.1.

Wu, Y., Chu, D., Tong, J., Song, H., Dal Corso, J., Wignall, P.B., Song, H., Du, Y., and Cui, Y., 2021, Six-fold increase of atmospheric $p\mathrm{CO_2}$ during the Permian–Triassic mass extinction: Nature Communications, v. 12, 2137, https://doi.org/10.1038/s41467-021-22298-7.

Yin, H., Huang, S., Zhang, K., Hansen, H., Yang, F., Ding, M., and Bie, X., 1992, The effects of volcanism on the Permo-Triassic mass extinction in South China, *in* Sweet, W.C., et al., eds., Permo-Triassic Events in the Eastern Tethys: Cambridge, UK, Cambridge University Press, p. 146–157.

Zhang, H., et al., 2021, Felsic volcanism as a factor driving the end-Permian mass extinction: Science Advances, v. 7, https://doi.org/10.1126/sciadv.abh1390.

Printed in the USA